

ACCEPTED MANUSCRIPT

A model of electrical impedance tomography implemented in nerve-cuff for neural-prosthetics control

To cite this article before publication: James Hope *et al* 2018 *Physiol. Meas.* in press <https://doi.org/10.1088/1361-6579/aab73a>

Manuscript version: Accepted Manuscript

Accepted Manuscript is "the version of the article accepted for publication including all changes made as a result of the peer review process, and which may also include the addition to the article by IOP Publishing of a header, an article ID, a cover sheet and/or an 'Accepted Manuscript' watermark, but excluding any other editing, typesetting or other changes made by IOP Publishing and/or its licensors"

This Accepted Manuscript is © 2018 Institute of Physics and Engineering in Medicine.

During the embargo period (the 12 month period from the publication of the Version of Record of this article), the Accepted Manuscript is fully protected by copyright and cannot be reused or reposted elsewhere.

As the Version of Record of this article is going to be / has been published on a subscription basis, this Accepted Manuscript is available for reuse under a CC BY-NC-ND 3.0 licence after the 12 month embargo period.

After the embargo period, everyone is permitted to use copy and redistribute this article for non-commercial purposes only, provided that they adhere to all the terms of the licence <https://creativecommons.org/licenses/by-nc-nd/3.0>

Although reasonable endeavours have been taken to obtain all necessary permissions from third parties to include their copyrighted content within this article, their full citation and copyright line may not be present in this Accepted Manuscript version. Before using any content from this article, please refer to the Version of Record on IOPscience once published for full citation and copyright details, as permissions will likely be required. All third party content is fully copyright protected, unless specifically stated otherwise in the figure caption in the Version of Record.

View the [article online](#) for updates and enhancements.

A model of electrical impedance tomography implemented in nerve-cuff for neural-prosthetics control.

J. Hope^{1,2}, F. Vanholsbeeck², A. McDaid¹

¹Department of Mechanical Engineering, The University of Auckland, 5 Grafton Road, Auckland 1010, NZ
²Dodd Walls Centre, The Department of Physics, The University of Auckland, 38 Princes Street, Auckland 1010, NZ

Abstract

Objective: In neural interfaces for peripheral nerve a trade-off exists between the level of invasiveness and the selectivity of neural recordings. In this study, we implement electrical impedance tomography (EIT) in a nerve cuff with the aim to investigate the achievable level of selectivity.

Approach: Established modelling approaches in neural-EIT are expanded on to be used, for the first time, on myelinated fibres which are abundant in mammalian peripheral nerves and transmit motor commands. The model is then used to evaluate the viability of using EIT with a nerve cuff to record neural activity in peripheral nerves.

Main results: Fibre impedance models indicate activity in unmyelinated fibres can be screened out from activity in myelinated fibres using operating frequencies above 100 Hz. At 1 kHz the transverse impedance magnitude, which is perpendicular to the fibre length axis, of inactive intra-fascicle tissue and the fraction change during neural activity are estimated to be 1,142 Ω .cm and -8.8×10^{-4} , respectively. At 1 kHz and 10 mm spacing between the impedance measurement electrode pair, the longitudinal impedance magnitude, which is parallel to the fibre length axis, and the fraction change during neural activity are estimated to be 328 Ω .cm and -0.30, respectively. We show that a novel EIT drive and measurement electrode pattern which utilises longitudinal current and longitudinal differential boundary voltage measurements could distinguish activity in different fascicles, as well as simultaneous activity in multiple fascicles, of a three-fascicle mammalian nerve using simulated data.

Significance: The results of this study provide an estimate of the transient change in impedance of intra-fascicle tissue during neural activity in mammalian nerve, and present a viable EIT electrode pattern, both of which are critical steps towards implementing EIT in a nerve cuff for a recording neural interface.

I. INTRODUCTION

Limb loss is projected to affect 2.2 million people in the USA by 2020, of which 35% of cases affect the upper limb (Ziegler-Graham, MacKenzie et al. 2008). Prosthetics offer a means to improve quality of life for amputees by restoring the lost functions needed to perform activities of daily life (Spiers, Resnik et al. 2017). However, modern electric prosthetics for transradial and transhumeral amputees contain more mechanical degrees of freedom than can be intuitively controlled due to limitations in the neural-interface (Grimmann and Dietl 2013). Increased dexterity/ functionality and increased control are two factors which are desired by users (Biddiss, Beaton et al. 2007, Engdahl, Chestek et al. 2017) and contribute to lowering user rejection rates (Østlie, Lesjø et al. 2012). A study by (Engdahl, Chestek et al. 2017) reported 64% of users are interested to test an implantable peripheral nerve interface (PNI) if it improves prosthetic functionality despite the medical risks associated with some PNI hardware.

Among PNI technologies, a trade-off exists between beneficial characteristics, with no single device achieving low invasiveness, high chronic stability, and a high number of control channels (selectivity) (Ortiz-Catalan, Brånemark et al. 2012, del Valle and Navarro 2013, Thompson, Zoratti et al. 2016). Desirable features of selectivity are the resolution of multiple, spatially separated, and concurrent signals present in the same fascicle or different fascicles of a multi-fascicle nerve. More invasive devices, such as microelectrode arrays and intra-fascicular electrodes, penetrate the fascicles to reduce the proximity between electrodes and the target fibre populations, and, in doing so, exhibit high selectivity. However, micromotion and tethering forces from wires, combined with a stiffness mismatch between neural tissue and the interface device, can lead to persistent inflammation in microelectrode arrays (Thompson, Zoratti et al. 2016) and fatigue failure in intra-fascicular devices (Yoshida, Farina et al. 2010), thus producing poor chronic stability. Nerve cuffs are the least invasive PNI

and exhibit high chronic stability, but are also the least selective PNI. Researchers have used nerve cuffs to identify touch force and slip (Haugland and Hoffer 1994, Haugland, Hoffer et al. 1994), estimate joint angle (Chan, Lin et al. 2012), and as a sensor in closed loop functional electrical stimulation (FES) systems (Haugland and Sinkjaer 1995, Haugland, Lickel et al. 1999, Inmann and Haugland 2004). While many researchers have shown it is possible to classify multiple concurrent signals based on the type of sensory information (Raspopovic, Carpaneto et al. 2010, Rieger and Taylor 2013, Al-Shueli, Clarke et al. 2014, Karimi and Seydnejad 2015), it has not been possible to differentiate more than two concurrent signals of the same type (Raspopovic, Carpaneto et al. 2010, Zariffa 2015), which is a major barrier to the use of nerve cuff for neural prosthetics control.

Electrical Impedance Tomography (EIT) is an imaging modality using electrical impedance as the contrast agent with biomedical applications in monitoring of respiratory and pulmonary systems (Frerichs, Amato et al. 2017), in identification of ischaemic brain tissue for diagnosis of stroke (Dowrick, Blochet et al. 2015), and in localisation of epileptic foci (Dowrick, Dos Santos et al. 2015, Aristovich, Packham et al. 2016) amongst others (Bayford, Ollmar et al. 2017). The application of EIT to a nerve cuff offers a potential means to classify multiple concurrent motor-command signals based on their location within the peripheral nerve. Somatotopic organisation of fibres and fascicles occurs in peripheral nerves in the form of bundling of fibres in proximal fascicles based on the distal point that they innervate (Jabaley 1980), and high concentration of fibres by function within some fascicles (Tyler, Polasek et al. 2015), giving promise to a tomographic approach to nerve cuffs for control of neural-prosthetics.

In differential EIT, transient changes in the impedance distribution within the sample acts as the contrast agent. The change in impedance of neural tissue during activity in neural cells is attributed to the increased membrane conductivity during action potentials (Holder 1992, Boone 1995). Neural-EIT has been developed using nerve fibre impedance models based on unmyelinated fibre membrane dynamics and single cable theory, and a crab nerve animal model in experiments (Holder 1992, Boone 1995, Liston 2003, Gilad, Ghosh et al. 2009, Oh, Gilad et al. 2011, Liston, Bayford et al. 2012, Aristovich, Dos Santos et al. 2015). Nerve fibre impedance models have been combined with physiological information on the mammalian brain to image cortical activity during sensory stimuli in humans (Davidson, Wright et al. 2010, Pomfrett, Davidson et al. 2010, McCann, Ahsan et al. 2011, Pollard, Pomfrett et al. 2011) and in rats (Aristovich, Santos et al. 2014, Vongerichten 2015, Aristovich, Packham et al. 2016, Vongerichten, dos Santos et al. 2016). In rat brain, spatial and temporal resolutions of 0.05mm & 2ms (Aristovich, Santos et al. 2014, Aristovich, Packham et al. 2016) and 0.4mm & 3.3ms (Vongerichten 2015, Vongerichten, dos Santos et al. 2016) were achieved, which if replicated on a nerve cuff would provide sub-fascicle level selectivity. Efforts to apply EIT to a nerve cuff have reported transient longitudinal impedance changes in the nerve, but not spatial reconstruction of neural activity, using four longitudinally spaced electrodes (Fouchard, Coizet et al. 2017). Furthermore, using a nerve cuff containing a multi-electrode array configured in a single ring, which is sensitive to transverse impedance changes, fascicle level selectivity in rat sciatic nerve (Aristovich 2016) and spontaneous activity of cardiac and pulmonary functions in vagus nerve of sheep (Aristovich 2017) has been reported.

In this study, we investigate the application of EIT to a nerve cuff for neural-prosthetics control. We applied, for the first time, modelling approaches for neural-EIT to myelinated fibres. This modelling produced estimates of anisotropic impedance of intra-fascicle tissue (fibres and extracellular space) which allows us to evaluate potential EIT drive and measurement electrode patterns. We investigate the expected performance of a novel EIT electrode pattern, implemented on a 32 channel dual-ring electrode array, for EIT reconstruction of neural activity in a multi-fascicle mammalian nerve using simulated data. The results provide insights into operating parameters and potential EIT electrode patterns in an experimental set-up, and the viability of a nerve-cuff based EIT interface for neural prosthetics.

II. METHODS

In accordance with other research we separated our model into three components (Boone and Holder 1995, Oh, Gilad et al. 2011, Liston, Bayford et al. 2012, Aristovich, Santos et al. 2014). The first component calculates transient changes to the conductivity of the nerve fibre membrane during propagation of an action potential using a Hodgkin-Huxley type model of ion channel behaviour (Hodgkin and Huxley 1952) or using empirical data. We extended existing models to account for myelinated fibres by first modelling the myelin sheath as a perfect insulator (Richardson, McIntyre et al. 2000). The second component calculates the specific impedance

of nerve fibre under an oscillating extracellular current by modelling the smallest repeating unit of a fibre in extracellular space with an equivalent electrical circuit, and then solving this model with cable-theory. We modified this for myelinated fibres by evaluating a single-cable model with lumped parameters, which allows direct application of impedance analysis techniques described in (Liston, Bayford et al. 2012), and a more physiologically accurate double cable model with non-uniform ion channel distribution (McIntyre, Richardson et al. 2002). We have split this second component into two sections in this paper, in order to address the transverse impedance, perpendicular to the fibre length axis, and the longitudinal impedance, parallel to the fibre length axis, separately. Separating the model into purely transverse and longitudinal impedance components provides a bulk approximation of the material anisotropy based on its smallest repeating unit. A bulk approximation assumes homogeneity of the material, which is biologically inaccurate at scales comparable to the smallest repeating unit of a nerve fibre, of several μm in the transverse direction and several 100's of μm in the longitudinal direction, but is considered sufficiently accurate for the purpose of modelling bulk response of neural tissue in EIT. The third component uses bulk tissue conductivities in a layered volume conductor model of the nerve that is solved using the finite element method (FEM) to estimate boundary voltage data from given tissue conductivity distributions. We based the morphology of our model on a three-fascicle rat sciatic nerve (Layton and Sastry 2004, Prodanov 2006).

The rat sciatic nerve offers similarities in morphology to the human median nerve which make it a suitable sample in PNI research for neural prosthetics. The rat sciatic nerve has 3 to 4 fascicles ranging in size from 0.05 to 1 mm^2 (from our own histology (Hope 2017)) each containing a heterogeneous distribution of motor fibres ranging in size from 10 to 15 μm (Prodanov 2006). In comparison, the median nerve in the human upper limb contains 10 or more fascicles at the elbow, which range in size from 0.12 to 2 mm^2 each containing a heterogeneous distribution of motor fibres ranging in size from 12 to 22 μm (Delgado-Martínez, Badia et al. 2016). All three major nerves which traverse the elbow in the human upper limb, the median, ulnar and radial, contain multi-fascicle morphology (Sunderland 1945) and innervate muscles which control the motor functions of the hand and wrist (Jabaley, Wallace et al. 1980).

A. Membrane Conductivity

For unmyelinated fibres, we calculated the membrane conductivity using the parameters and equations for rats and mice provided in a 2014 study (Neishabouri and Faisal 2014). In myelinated fibres, the ion channels on the node of Ranvier control the majority of the transmembrane ion-flux during the depolarisation phase of an action potential. Membrane conductivity at the node of Ranvier was calculated using parameters and equations from (Brazhe, Maksimov et al. 2011) as the sum of the fast Sodium, persistent Sodium, and slow Potassium ion channels, as well as the passive membrane leakage.

B. Transverse Fibre Impedance

Impedance models of an unmyelinated fibre are derived from assumptions that the membrane is a semi-conductive thin-walled cylinder of constant diameter which separates two conductive volumes, the intracellular fluid and extracellular space. In transverse orientation, the electric current is applied perpendicular to the fibre length axis, and, accordingly, in longitudinal orientation, the current is applied parallel to the fibre length axis.

The specific impedance of an unmyelinated fibre in a transverse current $z_{U,t}$ (Ωm) was calculated using equation 1 (Boone 1995):

$$z_{U,t} = r_e \frac{r_e(1-\alpha) + (r_i + \frac{z_m}{a_m})(1+\alpha)}{r_e(1+\alpha) + (r_i + \frac{z_m}{a_m})(1-\alpha)} \quad (1)$$

where α is the volume fraction of the fibre in extracellular space, a_m the membrane radius, r_e extracellular space resistivity (Ωm), and r_i intracellular fluid resistivity (Ωm). Membrane impedance is given by $z_m = \frac{r_m}{1+j\omega r_m c_m}$, where j is the imaginary operator, ω the angular frequency (rad/s), r_m membrane area resistivity (Ωm^2), c_m membrane area capacitance (Fm^{-2}).

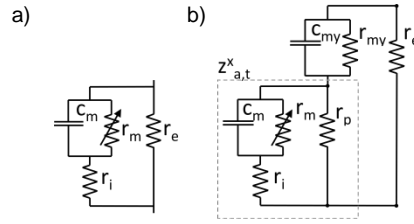


Figure 1: Transverse current equivalent electrical circuits of unmyelinated fibres and the node of Ranvier region in myelinated fibres (a), and the paranode, juxta-paranode and internode regions of myelinated fibres (b). In both models an oscillating current is applied across the extracellular resistance r_e to determine the circuit impedance.

The presence of Schwann cells around a myelinated fibre axon and variable ion channel concentration creates a more complicated cytostructure which must be reflected in the equivalent electrical circuits. The smallest repeating unit of a myelinated fibre extends between two neighbouring nodes of Ranvier, and can be broken down into four regions as described in (McIntyre, Richardson et al. 2002, Scherer and Arroyo 2002); these are 1) the node of Ranvier, which primarily contains fast Sodium ion channels; 2) the paranode, where the myelin sheath attaches to the axon; 3) the juxta-paranode which primarily contains fast Potassium and slow Potassium ion channels; and 4) the internode, with a relatively low concentration of ion channels.

The specific impedance of a myelinated fibre in the presence of a transverse current $z_{M,t}$ was calculated by summing the impedances of each region together in a 'parallel' configuration after weighting the values by their length fraction. Each length fraction was calculated as the region length divided by the node-to-node distance, using dimensional data from (McIntyre, Richardson et al. 2002). Specific transverse impedance of the node of Ranvier $z_{M,t}^n$ was calculated using equation 1. For the remaining regions, the specific impedance was calculated by first modifying the parameters in equation 1 to describe the axon in Periaxonal space:

$$z_{a,t}^x = r_p \frac{r_p(1-\alpha_a) + (r_i + z_m/a_m)(1+\alpha_a)}{r_p(1+\alpha_a) + (r_i + z_m/a_m)(1-\alpha_a)} \quad (2)$$

where superscript x indicates the region, r_p is the periaxonal space resistivity, and α_a is the volume fraction of axon in periaxonal space. The axon impedance was then nested inside a myelin sheath and extracellular space, see Fig 1, by again modifying the parameters in equation 1:

$$z_{M,t}^x = r_e \frac{r_e(1-\alpha_{my}) + (z_{a,t}^x + z_{my}/\tilde{a}_{my})(1+\alpha_{my})}{r_e(1+\alpha_{my}) + (z_{a,t}^x + z_{my}/\tilde{a}_{my})(1-\alpha_{my})} \quad (3)$$

where \tilde{a}_{my} is the average myelin radius, $z_{my} = \frac{r_{my}}{1+j\omega r_{my} c_{my}}$ as before but with the subscript my denoting myelin sheath properties, and α_{my} is the volume fraction of the axon and periaxonal space inside the myelin and extracellular space. Current is assumed to only flow radially within the myelin sheath and so the volume occupied by the myelin sheath was omitted when calculating α_{my} .

C. Longitudinal Fibre Impedance

The specific impedance of an unmyelinated fibre in a longitudinal current $z_{U,l}$ was calculated using equation 4 (Liston, Bayford et al. 2012):

$$z_{U,l} = \frac{r_i r_e}{[(1-\alpha)r_e + \alpha r_i]} + \frac{r_e^2(1-\alpha)}{\alpha[(1-\alpha)r_e + \alpha r_i](LF)} e^{-LF} \sinh(LF) \quad (4)$$

where the electrodes are separated along the fibre length by distance $2L$, and the parameter $F = \frac{\sqrt{1+j\omega\tau}}{\lambda}$ contains the time constant $\tau = r_m c_m$ and length constant $\lambda = \sqrt{\frac{a r_m}{2(r_i + r_e \frac{(1-\alpha)}{\alpha})}}$ from the standard cable equation, used to model the fibre.

The specific impedance of a myelinated fibre in the presence of a longitudinal current $z_{M,l}$ was calculated using two models. The first, termed the ‘physiological model’, segmented the fibre length into the four types of regions described earlier in section B. *Transverse Fibre Impedance*. Each region was separated into five layers, see Fig 2a. Three of the five layers were longitudinal current paths: the extracellular space, periaxonal space, and intracellular space. The remaining two layers were transverse current paths through the myelin and the axon membrane, which connected the longitudinal current paths and created a more physiologically accurate double cable type model.

The second longitudinal fibre model, termed the ‘lumped parameter model’, omitted the Periaxonal space and the axon membrane in the myelinated regions, creating a single cable model. In addition, the myelin layer in each region and the node of Ranvier membrane were represented, respectively, by a single resistor and a single capacitor in parallel, producing the same equivalent electrical circuit as was used in unmyelinated fibres, Fig 2b. The lumped parameter model can therefore be used with analysis techniques which were developed on unmyelinated fibres (Liston, Bayford et al. 2012), although with the caveat that unmyelinated fibres exhibit homogeneity along the fibre length axis, which is not true of myelinated fibres. The assumption of homogeneity in the lumped parameter model is reasonable provided the spacing between the impedance measurement electrode pair is several mm, i.e. several times larger than the length of the smallest repeating unit of a myelinated fibre.

Both longitudinal current models were built in the electronic circuit analysis software *LTspice* for a length of fibre extending between two neighbouring nodes of Ranvier using absolute resistance and capacitance values calculated for a $5.7\mu\text{m}$ diameter myelinated fibre from electrical properties in Table 1 and dimensions from (McIntyre, Richardson et al. 2002). The impedance of the single cable model was evaluated using equation 4.

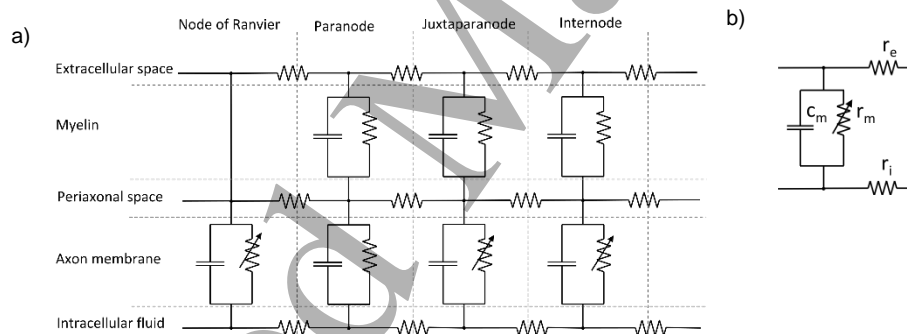


Figure 2: Part of the longitudinal current equivalent electrical circuit of the physiological model of a myelinated fibre (a) showing the five layers (extracellular space, myelin, periaxonal space, axon membrane, and intracellular fluid) and the four regions (node of Ranvier, paranode, juxtaparanode, and internode). Longitudinal current equivalent electrical circuit used for an unmyelinated fibre and for the lumped parameter model of the myelinated fibre (b). In both equivalent electrical circuits (a) & (b), an oscillating current is applied across the extracellular resistance to determine the circuit impedance.

D. Nerve Tissues

The change in the four fibre impedance parameters during neural activity ($\Delta z_{U,t}$, $\Delta z_{U,l}$, $\Delta z_{M,t}$, and $\Delta z_{M,l}$) were calculated using the two-state model approach outlined in (Liston, Bayford et al. 2012). The two state model calculates the fibre impedance in the active state using the maximum axon membrane conductivity attained during an action potential and then calculates the fraction change in impedance Δz_0 using $\Delta z_0 = \frac{z_{x,y}^d - z_{x,y}^p}{z_{x,y}^p}$, where subscripts x and y indicate the fibre type and orientation respectively, and superscripts d and p indicate the active (depolarised) and inactive (polarised) states respectively. The axon membrane conductivity in the active and inactive fibre states for unmyelinated fibres and the node of Ranvier region of myelinated fibres were calculated

as described earlier in *section A*. In myelinated fibre the axon membrane of the paranode region was assumed to have constant conductivity (McIntyre, Richardson et al. 2002), and in the juxtaparanode and internode regions axon membrane conductivity was calculated using ion channel concentration values from (Brazhe, Maksimov et al. 2011).

The fraction change in impedance of tissue in the intra-fascicle volume Δz_{IFV} was calculated by separating the range of fibre diameters present in the nerve into n sub-groups and summing them as in a 'parallel' configuration:

$$\frac{1}{\Delta z_{IFV}} = \sum_{i=1}^n \frac{T_{p,i} C_{p,i} V_i}{\Delta z_{0,i}} \quad (5)$$

where subscript i indicates the i^{th} fibre diameter sub-group, T_p and C_p are factors which correct for, respectively, the axon membrane capacitance and the fibre diameter dependent signal velocities. The volume fraction V_i of the i^{th} fibre group was calculated from fibre diameter population data for rat sciatic nerve in (Prodanov 2006). We assume a homogeneous fibre diameter distribution in our modelling, although, it is possible to input any values within the array of V_i values if this information is known a-priori about the sample. It is also possible, using equation 5, to customise which fibre diameter groups are active, as well as their level of activity, by varying the corresponding value of $\Delta z_{0,i}$, a useful feature when designing for specific neural prosthetics applications. In the current study all fibre diameter groups are assumed to be active.

The capacitance correction factor T_p was calculated as the difference in the maximum change in voltage between two parallel RC circuits as described in Ref (Liston, Bayford et al. 2012). One circuit had zero capacitance and the other a capacitance value taken from the lumped parameter fibre-model. For both circuits, the resistance changed as a function of time between that of the inactive and the active fibre states, with values again taken from the lumped parameter model. In myelinated fibres, the time varying function used was the falling edge of a sinusoidal signal with 12.5 kHz frequency, which was intended to approximate the 40 μ s rise time in membrane conductivity of the node of Ranvier during the depolarisation phase of an action potential. A sinusoid of 250Hz frequency was used to approximate the repolarisation phase. In unmyelinated fibres, the frequencies used for the depolarisation and repolarisation phases were 250 and 100 Hz respectively to approximate a 2ms rise time and 5ms fall time of the membrane conductivity during an action potential.

The signal velocity correction factor C_p was calculated as the product of signal dispersion effects and signal transit time effects. Signal dispersion accounts for the fibre diameter dependant propagation velocity of action potentials. In the context of an experiment, if all excitable neural tissue is excited at one point on the nerve and measured at another, the different propagation velocities will cause the signal to disperse based on the fibre diameter distribution. We assumed 30 mm between the source of the compound action potential and the proximal end of nerve cuff, within which signal dispersion occurred. Signal transit time effects accounted for the transient conductivity across the nodes of Ranvier within the nerve cuff, which, again, are caused, by the fibre diameter dependant propagation velocity. For each fibre, the nodes of Ranvier within the EIT imaging volume of the nerve cuff will be at different points of the transient depolarisation and repolarisation phases associated with an action potential. To account for this, for each fibre diameter group, we averaged the conductivity across all nodes of Ranvier within the imaging volume, then recalculated the corresponding fraction change in impedance and calculated the ratio against the scenario with no transit time effect. For longitudinal current an EIT imaging volume 10mm in length was assumed; in transverse current 2 mm length imaging volume was assumed.

Impedances of the passive tissues perineurium, epineurium and endoneurium obtained from mammalian peripheral nerves have not been reported before. Instead, it is common (as in (Choi, Cavanaugh et al. 2001, Yoo and Durand 2005, Kuhn 2008, Taghipour-Farshi, Frounchi et al. 2015, Garai, Koh et al. 2017)) to use value for perineurium (47,600 Ω .cm) obtained from frog (Weerasuriya, Spangler et al. 1984), and for epineurium (1,211 Ω .cm) from the transverse impedance of the dorsal column of cat at 1 kHz (Ranck Jr and BeMent 1965).

Endoneurium occupies the majority of the extracellular space within the intra-fascicle volume, with the remainder occupied by an approximately 40 – 100 nm thick layer of basal lamina immediately surrounding each fibre. The thickness of basal lamina was calculated from analysis of images in (Morris, Hudson et al. 1972, Geada Trigo Calheiros De Figueiredo 2014, Pannese 2015). Values in literature for the resistivity of extracellular space vary between 175 and 1,000 Ω .cm (Frijns and ten Kate 1994, Richardson, McIntyre et al. 2000, Kuhn 2008, Zariffa 2009). We adopted an isotropic resistivity of 1,000 Ω .cm which, using equations 1 – 4 at 1 kHz and 10mm longitudinal spacing between the impedance measurement electrode pair, produced transverse and longitudinal

resistivity values which were close to those reported in Ref (Ranck Jr and BeMent 1965) from the dorsal column of cat of 1,211 $\Omega\cdot\text{cm}$ radial and 138 to 217 $\Omega\cdot\text{cm}$ longitudinal.

E. Electrical Impedance Tomography Forward and Inverse Problems

The forward EIT problem is defined as $\mathbf{g}_n = \mathbf{A}\mathbf{c}_n$ where \mathbf{A} is the sensitivity matrix, and in neural EIT \mathbf{g}_n is the normalised change in boundary voltages and \mathbf{c}_n the normalised conductivity change (Holder 2004). The sensitivity matrix is populated from boundary voltages generated from known currents in a Finite Element Method (FEM) model simulation of the system (Holder 2004, Aristovich, Santos et al. 2014). The FEM model requires knowledge of the size, shape and location of the electrode array, and, if possible, some a-priori information on the conductivity distribution of the sample. Our nerve cuff electrode array contained a total of 32 electrodes, each 1.1 x 0.1mm, arranged into two rings of 16 electrodes on a 22.5° pitch around the circumference, Fig 3. For our sample volume we used a single fascicle model of a 50mm length by 680 μm diameter peripheral nerve comprised of four cylindrical layers: an 80 μm thick saline fluid layer between the electrodes and nerve outer boundary, 50 μm thick epineurium layer (Dumanian, McClinton et al. 1999), 5 μm perineurium layer (Layton and Sastry 2004), and a 545 μm radius intra-fascicle volume in the centre. Electrodes were then housed within a 120 μm thick silicon layer, 20mm in length, representing the nerve cuff, and the model was surrounded by a 200 μm thick layer of muscle tissue, not shown in Fig 3. We divided the intra-fascicle volume into a grid of 49 sub-volumes which extended the length of the nerve, Fig 3. The forward problem was then solved with each of the 49 sub-volumes individually set to an active state. A single fascicle model is akin to assuming no a-priori information about the intra-fascicle structure of the nerve.

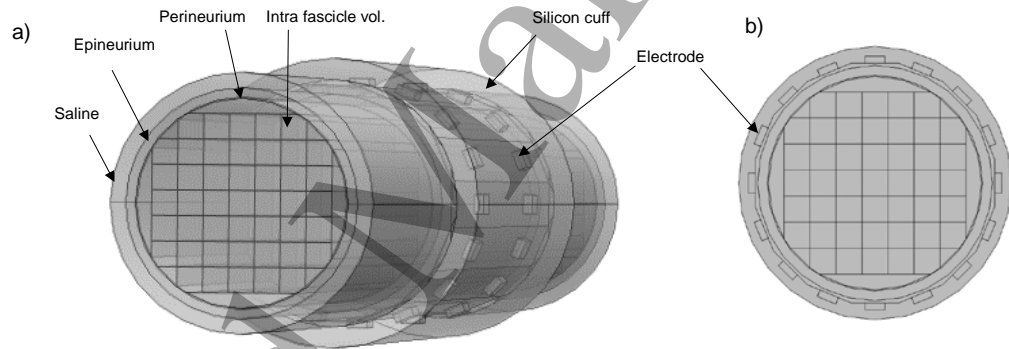


Figure 3: Two rings, each containing 16 electrodes, are spaced apart along the nerve length and wrapped around the cylindrical shell model of the nerve with layers for the saline fluid, epineurium, perineurium, and intra-fascicle sub-volumes visible in an angled end-and-side view of the FEM model (a) and in an end view of the FEM model (b) which has all 16 electrodes of one electrode ring visible.

For the inverse EIT problem we used Zeroth order Tikhonov regularisation to invert the sensitivity matrix as was done in neural-EIT experiments in (Aristovich, Santos et al. 2014, Vongerichten, dos Santos et al. 2016). The Tikhonov solution to the general inverse equation $\mathbf{c}_\tau = \mathbf{A}^\dagger \mathbf{g}$ is given by:

$$\mathbf{c}_\tau = \mathbf{V}\mathbf{F}\mathbf{\Sigma}^\dagger\mathbf{U}^\text{T}\mathbf{g} \quad (6)$$

where \mathbf{V} and \mathbf{U} are orthogonal matrices from singular value decomposition (SVD) regularisation of the sensitivity matrix $\mathbf{A} = \mathbf{U}\mathbf{\Sigma}\mathbf{V}^\dagger$, $\mathbf{\Sigma}$ is the diagonal matrix of singular values s_i , * indicates the Hermitian, and \mathbf{F} is a diagonal matrix where $F_{i,i} = s_i^2 / (s_i^2 + \tau^2)$. The L-curve, or Pareto frontier curve, method was used as an unbiased means to select the Tikhonov regularisation parameter τ (Nasehi Tehrani, McEwan et al. 2012).

Unbiased parameter selection is one of several recommendations made in (Holder 2004) to avoid committing an ‘inverse crime’ when using simulated instead of real data in inverse problems. Other recommendations that were implemented are: 1) Mesh size: our forward problem was meshed with a max mesh size of 4mm, a min mesh size of 0.1mm, a max growth rate of 1.3, a curvature factor of 0.2, and a resolution of narrow regions of 1. Our simulated data were acquired with the max and min mesh sizes reduced to 2mm and 0.05mm respectively. 2) Shape of conductivity anomalies: we generated simulated data on a three-fascicle model of nerve containing one semi-circular fascicle and two smaller quarter-circle shaped fascicles of equal size, Fig

4c. Each fascicle was encompassed by a 5 μm thick perineurium layer and separated by a 90 μm thick epineurium layer. Thus, the geometry and location of the epineurium, perineurium and intra-fascicle tissues in the three-fascicle model differs from the single fascicle model. However, in both models a 70 μm thick saline fluid layer, of 2 S/m conductivity, separated the electrodes and nerve outer boundary, and the epineurium-saline boundary had the same size and location. 3) Simulating noise: white noise of $\pm 35\mu\text{V}_{\text{RMS}}$ amplitude and Gaussian distribution was added to each simulated voltage measurement. 4) Hardware errors: a number within the range $\pm 100\mu\text{V}$ was randomly selected and added to each electrode pair as a fixed offset, which was intended to account for accuracy of the ADC hardware and electrode impedance measurement errors. 5) Quantization: all values were rounded to the nearest multiple of $10\mu\text{V}$.

The FEM models were implemented and solved within COMSOL Multiphysics version 5.3 AC/DC module on a Dell Optiplex 7040 PC with Intel i7-6700 processor. The single fascicle and multi-fascicle models contained 850k and 5.5M free tetrahedral elements respectively. The minimum and average mesh qualities were 3×10^{-2} and 0.56, respectively, for the single fascicle model, and 7.0×10^{-2} and 0.62, respectively, for the multi-fascicle model. In the multi-fascicle model the elements with poorest mesh quality, i.e. >0.1 , were limited to the 5 μm thick perineurium layer, which itself had an average mesh quality of 0.11. In the 32 electrode dual-ring nerve cuff there are a total of 16 possible drive electrode pairs for each longitudinal current pattern. In each drive current electrode pair, we applied a 10 μA amplitude (Fouchard, Coizet et al. 2017) drive current on the external surface of one drive electrode as a Neumann boundary condition, and grounded the external surface of the other drive electrode as a Dirichlet boundary condition. The muscle tissue layer, with conductivities of 0.3 and 0.1 S/m in the longitudinal and transverse axes respectively (Gielen, Wallinga-de Jonge et al. 1984), was defined as an infinite element domain. All electrodes had a conductivity of 4×10^6 S/m and contact impedance at the electrode-saline interface of $1.5 \times 10^{-4} \Omega\text{m}^2$. The recorded voltage from each measurement electrode was calculated as the averaged value across its external surface. Implementation of the above measures in the FEM models produce the discretization, shunt and contact impedance effects which constitute the complete electrode model (Holder 2004).

A quasi-static approximation of Maxwell's equations was implemented by solving the FEM models under several static conditions. In each condition the electrical conductivity of fascicle sub-volumes was set to that of either the active or inactive states. This quasi-static approach is valid for 'low frequency' drive currents, which was estimated using equation 7:

$$\omega \leq k \frac{\sigma}{\epsilon} \quad (7)$$

where ω is in rad/s, and k is a constant of less than 1 which determines the 'low frequency' limit, which we set to 0.1. The relative permittivity, ϵ , was taken as that of brain tissue (Gun, Ning et al. 2017) and the conductivity, σ , of intra-fascicle tissue was calculated from equation 5.

F. Electrical Impedance Tomography Electrode Drive and Measurement Pattern

We imposed a limit of one drive current pattern within the nerve cuff due to the millisecond to sub-millisecond time resolution required to resolve compound action potentials (Aristovich, Packham et al. 2016, Vongerichten, dos Santos et al. 2016) and the necessity to repeat the drive current pattern for all electrode pairs in each time resolution unit.

The nerve cuff with dual-ring electrode array can pass current between two drive electrodes on the same electrode-ring to generate transverse current patterns, or pass current between two drive electrodes on different electrode-rings to generate longitudinal current patterns, Fig 4. Simulations by (Graham and Adler 2007) compared seven possible drive current patterns within a dual-ring electrode array around a cylindrical sample volume with isotropic conductivity features for 3D EIT lung imaging of the thorax, concluding that transverse current pattern with drive current and voltage measurement between adjacent electrodes provided the best performance. Transverse current in a nerve would largely eliminate the anisotropy by operating in a plane perpendicular to the axis containing the unique conductivity, which we term the 'anisotropic axis', an approach adopted by (Aristovich 2016) on peripheral nerve and (Silva, Sousa et al. 2014) on muscle tissue.

Longitudinal current, on the other hand, in the dual-ring nerve cuff requires a 3D model and consideration of tissue anisotropy. Anisotropic conductivity anomalies produce boundary voltage data with non-unique solution (Adler, Gaburro et al. 2015), however, numerical methods with some a-priori information have proven capable of reconstructing anisotropic anomalies in 2D simulations (Hamilton, Lassas et al. 2014, Adler, Gaburro et al. 2015,

Wang, Xu et al. 2015) and in 3D simulations to manage anisotropy of white matter in the brain (Turovets, Volkov et al. 2014). The intention of longitudinal drive current is to exploit the impedance change in the longitudinal, anisotropic axis. However, configuration of the two electrode rings in the dual-ring nerve cuff, on planes perpendicular to the longitudinal axis, results in an EIT drive current with both transverse and longitudinal components, as shown by the equipotential lines in Fig 4b. In this study, the contribution to the EIT boundary voltages of the transverse and longitudinal current components have not been considered separately.

The unique combination of factors in our sample – differential 3D-EIT using dual-ring electrode array to detect conductivity variation in an anisotropic axis perpendicular to the planes of the electrode-rings – means there is no precedent for EIT drive and measurement electrode pattern. We propose a novel approach: to assume that transient conductivity variations of all tissues are uniform along the nerve’s length dimension, which is the anisotropic axis in intra-fascicle tissue, to simplify reconstruction of the conductivity distribution to a 2D plane perpendicular to the longitudinal current.

The use of opposing electrode positions for drive current, where the two drive electrodes are on opposite sides of the sample, has been employed to reduce a current channelling effect present in the cerebrospinal fluid when imaging neural activity in the brain (Bayford 2006). We did not consider In-line electrode positions for drive current, where the two drive electrodes are on the same circumferential position and different electrode rings, as we predict a similar effect in the saline fluid layer of our model. We considered one possible longitudinal drive current pattern as in Fig 4b: Opposing drive pattern, where drive current flows between two electrodes on opposite sides of the nerve and different electrode rings, generating a current with longitudinal components between the two electrode rings. In contrast to the convention in (Graham and Adler 2007), to record boundary voltages as differential measurements between electrode pairs configured in the same way as the drive current electrodes, we implemented our measurement electrode pairs in an in-line pattern in order to record the longitudinal boundary voltage gradients across the imaging volume. To abbreviate we refer to this electrode pattern with opposing drive electrode pair and in-line measurement pairs as ‘Opposing-in-line’.

The drive and measurement electrode pattern to use for EIT modelling was selected to maximise the sensitivity to changes in conductivity in the 9 central grids (3 x 3 squares) which produce the lowest changes in boundary voltages and so, accordingly, are most difficult to detect (Holder 2004). Sensitivity was defined as the standard deviation of the normalised change in boundary voltages (Fan, Wang et al. 2015), in our case in response to conductivity changes across the set of 9 central grids.

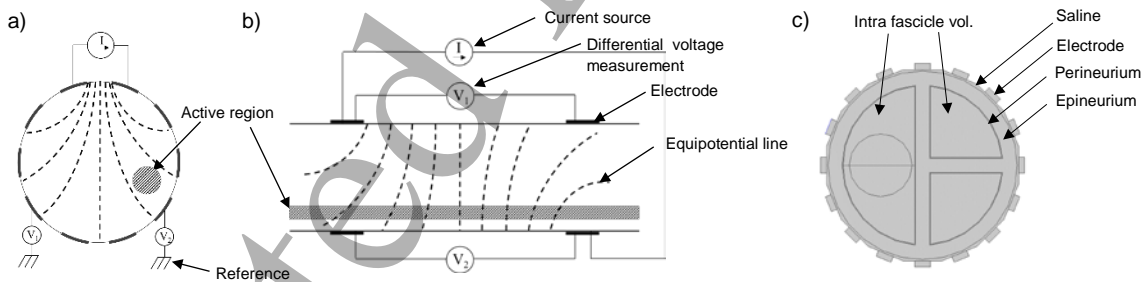


Figure 4: Section views of a possible transverse current pattern (a), and Opposing-in-line electrode pattern (b), with one opposing drive electrode pair and two in-line measurement electrode pairs visible. End view of the three fascicle model used to generate simulated data (c).

III. RESULTS

Table 1: Electrical properties values used in unmyelinated and myelinated nerve fibre models.

Parameter	Fixed value	Maximum	Minimum	Units
Unmyelinated				
Membrane conductivity		0.0008	0.000144	S/cm ²
Membrane specific capacitance	0.81			uF/cm ²
Myelinated				
Membrane conductivity in the regions				
Node of Ranvier		1.95	0.018	S/cm ²
Paranode	0.001			S/cm ²
Juxtaparanode		0.0082	0.002	S/cm ²
Internode		0.00269	0.002	S/cm ²
Membrane specific capacitance	2			uF/cm ²
Myelin specific capacitance per lamella (2 membranes)	0.05			uF/cm ²
Myelin conductivity per lamella (2 membranes)	0.0005			S/cm ²
Fluid and extracellular volumes				
Intracellular fluid resistivity	70			Ω.cm
Periaxonal fluid resistivity	70			Ω.cm
Extracellular space resistivity	1,000			Ω.cm
Extracellular space volume fraction (with myelin volume excluded)	0.5 (0.677)			

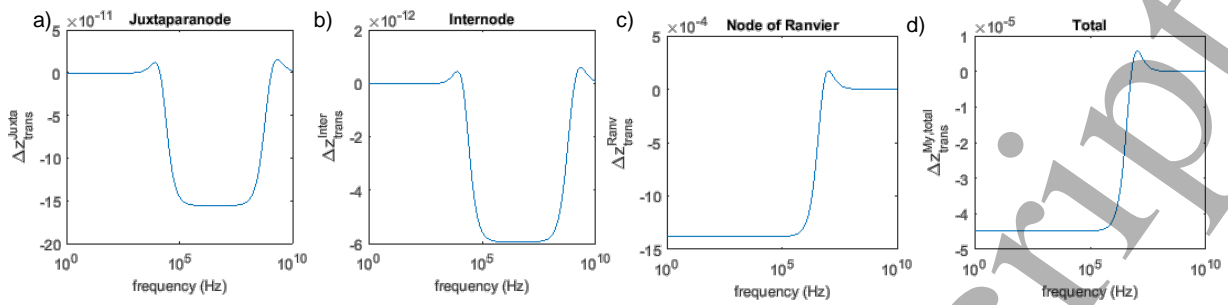
A. Membrane Conductivity

Membrane dynamics modelling showed that during an action potential both the relative increase in membrane conductivity and the maximum value reached are significantly higher in myelinated fibres, particularly at the node of Ranvier, than in unmyelinated fibres, see values in Table 1. Higher membrane conductivity is attributable to higher concentration of ion channels and facilitates a higher transmembrane ion flux, which, evidently, for Sodium ions was estimated to peak at around -33 mA/cm² in the node of Ranvier compared to -0.045 mA/cm² in an unmyelinated fibre. In an unmyelinated fibre, the maximum membrane conductivity increases by a factor of 5.56 up to a maximum value of 0.0008 S/cm². In a myelinated fibre, the node of Ranvier produces both the highest increase in conductivity, a factor of 108, as well as the highest maximum conductivity value of 1.95 S/cm². In comparison, the juxtaparanode changes by a factor of 4.1 to reach a maximum value of 0.0082 S/cm², and the internode changes by a factor of 1.35 to reach a maximum value of 0.00269 S/cm². The membrane surface area of the node of Ranvier is 2 to 3 and 3 to 4 orders of magnitude smaller than the juxtaparanode and internode regions respectively. Taken in this context, the significantly higher membrane conductivity of the node of Ranvier is explained by necessity to enable a large current through a relatively small area, i.e. a high transmembrane ion flux, during an action potential.

B. Transverse Fibre Impedance

For a myelinated fibre of 10 μm diameter (and 3 to 15 μm range), fraction change in transverse impedance of -1.6×10^{-10} (-4.6×10^{-11} to -2.3×10^{-10}) was predicted in the juxtaparanode region, and -5.9×10^{-12} (-1.8×10^{-12} to -8.9×10^{-12}) in the internode region, Table 2, Fig 5a & 5b. In contrast, in the node of Ranvier a fraction change of -1.4×10^{-3} (-4.3×10^{-4} to -2.0×10^{-3}) was predicted, which dominated the overall response of the fibre despite accounting for only 0.087% (0.33 to 0.069 %) of the total fibre volume, Table 2, Fig 5c & 5d. In the myelinated regions, the high resistance myelin sheath acts to shield the axon from the extracellular current. At frequencies above approximately 10⁹ Hz at which capacitive current traverses the myelin sheath, capacitive current also traverses the axon membrane, producing negligible changes in resistivity at all frequencies and rendering

changes in the axon membrane conductivity essentially undetectable. The unmyelinated node of Ranvier, on the other hand, shows a reasonable change in impedance magnitude below approximately 10^6 Hz, above which capacitive current traverses the axon membrane. An error of unknown magnitude will arise from treating the fibre



regions as separate 2D entities that are only connected by longitudinal current pathways in the extracellular space, as opposed to a 3D model with several transverse and longitudinal current pathways.

Figure 5: Frequency response of the fraction change in transverse impedance for the juxtaparanode (a), internode (b), and node of Ranvier (c) regions for a 15 μ m diameter myelinated fibre, and their combined transverse impedance corresponding to half of a node-node length (d). The node of Ranvier dominates the overall response despite accounting for the smallest volume fraction of the fibre.

The fraction change in transverse impedance of an unmyelinated fibre of 1.5 μ m diameter was estimated to be -1.4×10^{-4} at frequencies below 10^4 Hz. A frequency drop off, due to capacitive current traversing the axon membrane, begins at 10^5 Hz, an order of magnitude lower than for myelinated fibres, and settles at approximately 5×10^7 Hz after an incursion into positive fraction changes in impedance which peaks at 5.8×10^{-5} at 1.7×10^6 Hz. Frequency drop off values are in broad agreement with modelling on unmyelinated crab nerves, which spanned the frequency range 0 Hz (DC) up to 3×10^8 Hz, presented in (Boone 1995). The fraction change in transverse impedance in unmyelinated fibres is larger, by a factor of 3 or more, than all modelled diameters of myelinated fibres with the exception a small frequency range (5×10^5 to 10^6 Hz) where the curves intersect, Fig 6. Outside of this narrow frequency range activity in unmyelinated fibres would disproportionately affect detected impedance changes in intra-fascicle tissue when using transverse current in neural-EIT.

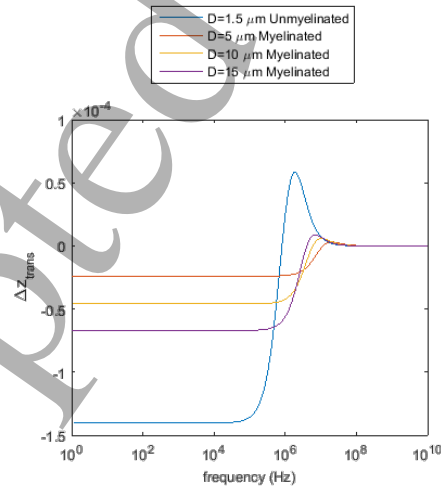


Figure 6: Frequency response of the fraction change in transverse impedance for unmyelinated and myelinated fibres. The fraction change is larger in unmyelinated fibres than in myelinated fibres at all frequencies except for the range 5×10^5 to 10^6 Hz.

Table 2: Maximum fraction change in transverse impedance.

	Unmyelinated	Myelinated	Myelinated	Myelinated
Diameter (μm):	1.5	3	10	15
Fibre segment (frequency range)				
Juxtaparanode (10^5 to 10^8 Hz)		-4.6×10^{-11}	-1.6×10^{-10}	-2.3×10^{-10}
Internode (10^5 to 10^8 Hz)		1.8×10^{-12}	-5.9×10^{-12}	-8.9×10^{-12}
Node of Ranvier ($<10^6$ Hz)		-4.3×10^{-4}	-1.4×10^{-3}	-2.0×10^{-3}
Entire myelinated fibre ($<10^6$ Hz)		-1.4×10^{-5}	-4.5×10^{-5}	-6.6×10^{-5}
Entire unmyelinated fibre ($<10^5$ Hz)	-1.4×10^{-4}			

C. Longitudinal Fibre Impedance

For longitudinal fibre orientation, *LTSpice* software was used to compare the lumped parameter model and the physiological model using absolute resistance and capacitance component values for a single length of myelinated fibre extending between two neighbouring nodes of Ranvier. At frequencies below 10^4 Hz the lumped parameter model produced an impedance magnitude which was higher than that of the physiological model by a factor of 1.4 to 1.9 in the inactive state and by a factor of 1.01 to 1.03 in the active state, Fig 7. There is a noticeable discrepancy between the two models in the shape of the curves at around 10^4 Hz, where the physiological model contains two additional inflection points closely spaced together, which can be attributed to capacitive current crossing the axon membrane in the myelinated regions. The observed differences between the two models are caused by current entering the periaxonal space longitudinally between the node of Ranvier and paranode regions, particularly in the inactive state. We believe that the value used for the resistance which controls longitudinal current between the node of Ranvier and paranode regions is too high. This belief is supported qualitatively by accumulation of potassium ions and swelling in the paranodes during sustained activity observed in (Geada Trigo Calheiros De Figueiredo 2014).

Equation 4 predicted significant differences in the frequency response between unmyelinated fibres and the lumped parameter model of myelinated fibres as seen in Figs. 8a and 8b. In unmyelinated fibres and 10mm electrode spacing, the largest fraction change was -0.10 at 1 Hz. The frequency drop off caused by capacitive current across the axon membrane began at 1 Hz and settled around at 300 Hz after an incursion into the positive range, which peaked with a value of 3.9×10^{-3} at 100 Hz, Fig. 8a. In myelinated fibres, for all diameters the frequency drop off began at around 200 Hz and settled to zero at 1 MHz after an incursion into positive values beginning at around 100 kHz, Fig. 8a. Higher frequency drop off values in myelinated fibres are expected due to the presence of the lower capacitance myelin sheath. The largest fraction change for all myelinated fibre diameters were observed below 200 Hz. The magnitude of the fraction change increased with increasing fibre diameter, and with decreasing electrode spacing down to 3 mm, Fig. 8b. The electrode spacing is, therefore, a variable which may be selected to exploit sensitivity to larger fibre diameters, responsible for motor command functions, in neural prosthetic applications. At 1mm electrode spacing the magnitude of the fraction change decreased with increasing fibre diameter. However, below 3mm the electrode spacing is comparable to the node to node distance of large diameter fibres, invalidating the assumption of homogeneity in the lumped parameter model. The frequency at which the frequency drop off begins changed negligibly across different fibre diameters and electrode spacing. The difference in the frequency drop off between unmyelinated and myelinated fibres indicates it is possible to screen out unmyelinated fibre activity using the operating frequency, and to distinguish their activity using multi-frequency EIT.

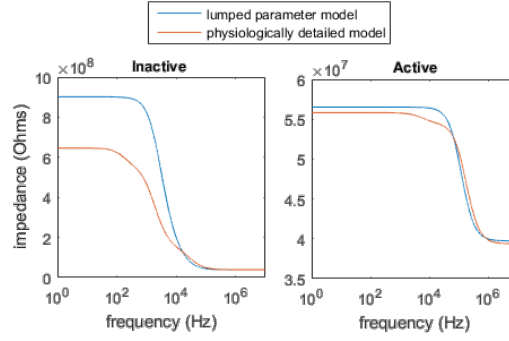


Figure 7: Impedance of the lumped parameter model and physiologically detailed model for a myelinated fibre in inactive (left) and active (right) states. There is a significant difference between the two models in the inactive fibre state at frequencies below 10^4 Hz, and good agreement between the two models in the active state at all frequencies.

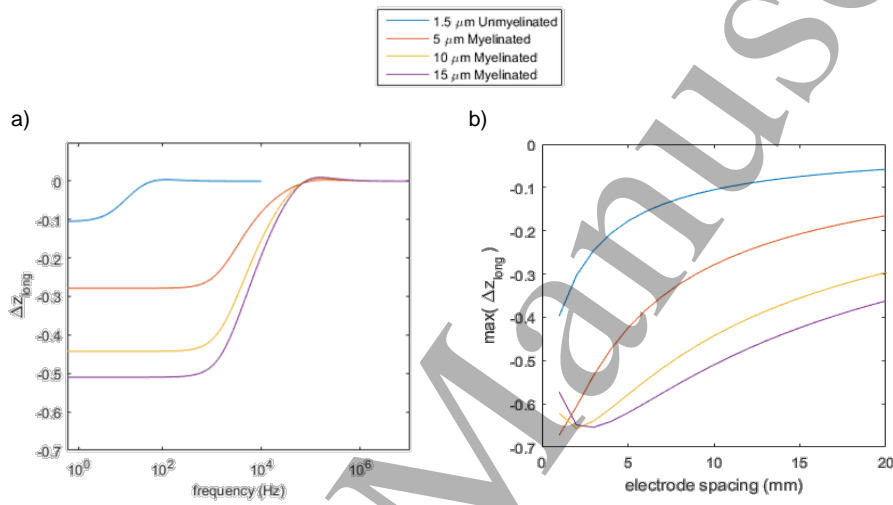


Figure 8: Frequency response of the fraction change in longitudinal impedance for unmyelinated and lumped parameter model of myelinated fibres at 10 mm electrode spacing (a). The frequency drop off occurs at much lower frequency in unmyelinated fibres than in myelinated fibres. The maximum fraction change in longitudinal impedance, which occurs at 1 Hz, shows dependence on electrode spacing and fibre diameter (b).

D. Nerve Tissues

The time constants of a $1.5 \mu\text{m}$ diameter unmyelinated fibre were 2.5 ms in the active state and 14 ms in the inactive state; producing a capacitance correction factor T_p of 2.8. In contrast, lumped parameter model values of a $10 \mu\text{m}$ diameter myelinated fibre produced time constants of 1.61×10^{-2} ms in the active state and 1.05 ms in the inactive state, with little variation from these values for other fibre diameters; T_p was 1.00. In the velocity correction factor C_p , transit time effects through the nerve cuff were found to be negligible due to the high signal velocities in myelinated fibres and significant drop in resistance at the active nodes of Ranvier. Signal dispersion effects reduced the fraction change in impedance by a factor of 1.16 over 30 mm travel distance, increasing to a factor of 1.94 over 100 mm. Dispersion correction is most relevant to an experimental set-up with controlled nerve excitation, where the travel distance is known.

At 1 kHz the estimated impedance magnitude of intra-fascicle tissue reduced from $1,142 \Omega \cdot \text{cm}$ (inactive) to $1,141 \Omega \cdot \text{cm}$ (active) in the transverse orientation, a fraction change of -8.8×10^{-4} , and from $328 \Omega \cdot \text{cm}$ (inactive) to $230 \Omega \cdot \text{cm}$ (active) in longitudinal orientation, a fraction change of -0.30. For comparison, impedance values reported in (Ranck Jr and BeMent 1965) from in-vivo measurements on the dorsal column of cat, at 1 kHz and 10 mm electrode spacing, are $1,211 \Omega \cdot \text{cm}$ transverse and 138 to $217 \Omega \cdot \text{cm}$ longitudinal, Table 3. The peripheral nerve is not directly comparable to the dorsal column because the latter is part of the central nervous system and so contains neurones and additional types of glial cells (Pannese 2015). In addition, the experiments on dorsal column

were performed in-vivo, under sodium barbiturate anaesthetic, and so may include both active and inactive neurones and nerve fibres.

Table 3: Longitudinal impedance values of intra-fascicle tissue at 1 kHz. The state of the neural tissue, i.e. active, inactive or mixed, is unknown in the experimental data of (Ranck Jr and BeMent 1965)

	Model prediction	Cat dorsal column (Ranck Jr and BeMent 1965)	units
Transverse	1,142 (inactive) / 1,141 (active)	1,211 (unknown state)	$\Omega\cdot\text{cm}$
Longitudinal	328 (inactive) / 230 (active)	138 to 217 (unknown state)	$\Omega\cdot\text{cm}$

E. Electrical Impedance Tomography

The quasi-static approximation of Maxwell's equations was determined, using equation 7, to be valid at frequencies of several 100's of kHz and below. This frequency range is useful in neural EIT as it coincides with the initial resistivity plateau, where the phase is small and capacitive charge transfer across the cell membrane is absent, which occurs with longitudinal currents below 5 kHz in the myelinated dorsal column of cat (Ranck Jr and BeMent 1965) and below 100 Hz for the unmyelinated crab nerve.

Sensitivity analysis of the electrode patterns produced standard deviations across the normalised boundary voltage measurements of 3.37×10^{-5} for transverse current pattern with drive current and voltage measurement between adjacent electrodes, and 1.28×10^{-4} for Opposing-in-line pattern at 10 mm electrode spacing increasing to 2.67×10^{-4} at 3 mm electrode spacing; we therefore selected Opposing-in-line pattern.

In Opposing-in-line pattern, due to the increased resistance between the two current electrodes, both the voltage across the drive current electrodes and the signal to error ratio (SER), which is the combined effect of the upper limit of the assumed noise and errors and is calculated using normalised values, increases with increasing electrode spacing. The SER of the normalised change in differential voltages increased by a factor of 6.7 between electrode spacings of 3 mm and 10 mm, and by a factor of 3.1 between electrode spacings of 6 mm and 10 mm. Referring back to Fig 8, when selecting the electrode spacing a trade-off exists between the fraction change in impedance and the SER. Incidentally, in neural EIT experiments researchers have typically averaged recordings across multiple measurements to reduce noise (Aristovich, Dos Santos et al. 2015, Aristovich 2016, Vongerichten, dos Santos et al. 2016, Fouchard, Coizet et al. 2017). Averaging cannot be implemented in real-time imaging, a crucial requirement for a neural prosthetics control interface, and so has not been assumed in our model.

With 10 mm electrode spacing EIT of activity in each fascicle of the three fascicle model were clearly distinguishable from one another by the levels of reconstructed activity in different sub-volumes, Fig 9. Concurrent activity was clearly distinguishable from individual activity in fascicles 2 and 3, Fig 9. EIT of sub-fascicle activity within fascicle 1 reconstructed different magnitudes of activity in the same sub-volumes, indicating poor intra-fascicle resolution. The ability to distinguish between concurrent and individual activity in different fascicles, and between activity in different areas within the same fascicle, are both critical requirements for neural prosthetics due to the multi-fascicular structure and heterogeneous distribution of fibres in human nerves. The limited intra-fascicle resolution may be improved by a higher number of sub-volumes used in the forward solution, improved FEM mesh quality in the perineurium layer, reduced noise and errors, inclusion of passive tissue structures in the forward solution (Jehl, Aristovich et al. 2016), and use of additional reconstruction steps in solving the inverse problem (Aristovich, Santos et al. 2014). SERs in the normalised change in differential voltages were 23 in semicircle shaped fascicle 1, and 16 in the two quarter-circle shaped fascicles 2 and 3, indicating real-time imaging of fascicle level activity is achievable in experiments on rat sciatic nerve at the assumed noise and error levels.

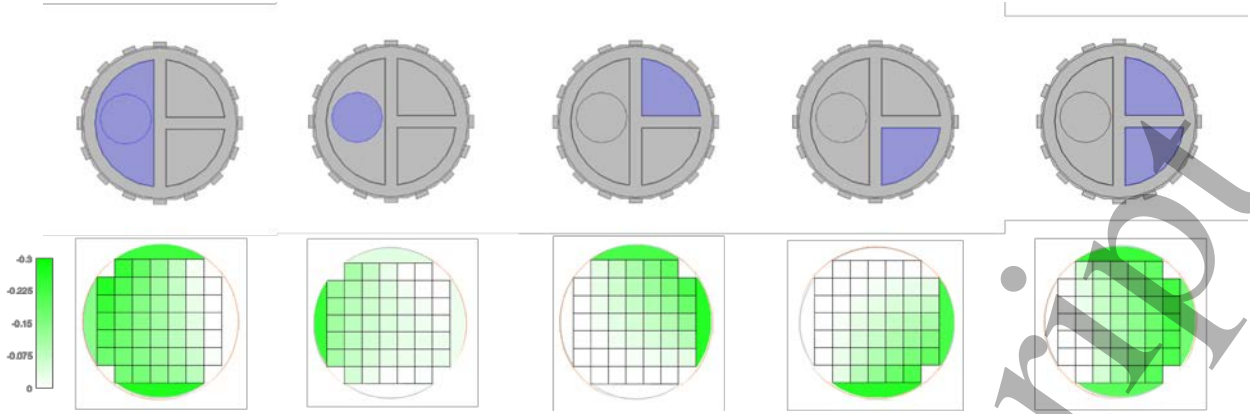


Figure 9: Activity in the three fascicle model (top row), with purple indicating -0.286 fraction change in longitudinal impedance, and the corresponding reconstruction using the EIT algorithm, which was populated with data from the single-fascicle model, (bottom row) with colour scale showing fraction change in impedance.

IV. DISCUSSION

The inclusion of passive tissues and a saline fluid layer in our model, to better describe the response of a whole nerve, reduces the fraction change in impedance. The extent of this reduction depends on the thickness of the passive tissue and saline fluid layers. For comparison, results of impedance experiments on rat sciatic nerve by Ref (Fouchard, Coizet et al. 2017) reported an undetectable fraction change in transverse impedance in the frequency range 100 Hz to 4.5 kHz, and a frequency dependent longitudinal fraction change in impedance with maximum value of -0.2 and frequency drop off beginning at approximately 200 Hz, see Fig 10. These experiment results are in reasonable agreement with our model prediction. More experiment data is required for a direct comparison, some of which, e.g. saline fluid layer thickness, cannot be easily determined.

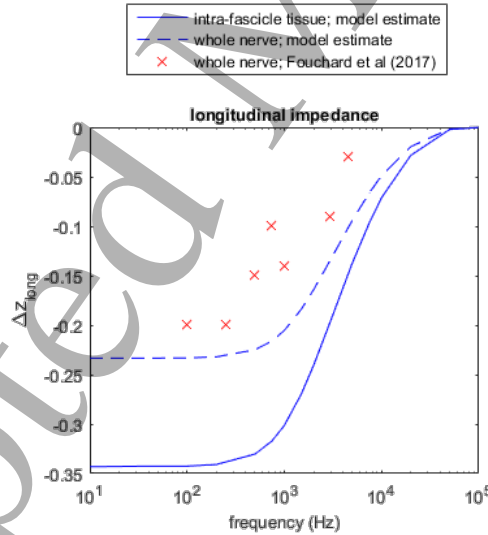


Figure 10: The fraction change in longitudinal impedance is lower for the whole nerve than for the intra-fascicle tissue as the whole nerve includes passive tissues and saline layer. Shape and magnitude of the curve for whole nerve shows reasonable agreement with Fouchard et al (2017).

For control of neural prosthetics, we may consider a scenario where only certain types of fibres are active in each sub-volume of intra-fascicle tissue. Applying activity only in motor-command fibres to equation 5, using the statistical classification of fibres in (Prodanov 2006), reduces the expected fraction change in longitudinal impedance of intra-fascicle tissue to a maximum of -0.14 at 1 Hz (-0.12 at 1 kHz). Assuming an average asynchronous firing rate of 25 Hz across all motor fibres in an intra-fascicle tissue sub-volume, taken from motor unit firing rates associated with movement in the upper limb (Farina, Rehbaum et al. 2014), the expected fraction

change in longitudinal impedance is -0.007 at 1 Hz (-0.006 at 1 kHz). While these magnitudes are relatively small they are not prohibitive to EIT imaging, in fact, they are comparable to fraction impedance changes observed in neural tissue in the cerebral cortex (unmyelinated grey matter) of rat of between -0.01 (DC) and -0.001 (10kHz) (Oh, Gilad et al. 2011) which have been successfully reconstructed using neural EIT by (Aristovich, Packham et al. 2016). Somatotopic organisation of fibres within fascicles would increase the magnitude of impedance change.

We have shown that EIT within a dual-ring electrode array operating with an Opposing-in-line pattern can produce fascicle level selectivity, with both individual and multiple fascicles active, in a 3 fascicle model of rat sciatic nerve. Spatial selectivity of sub-fascicle activity, however, was poorly reconstructed. Reconstruction of fascicle level activity in all fascicles of the human median nerve, containing e.g. 10 fascicles at the elbow, would provide a level of selectivity sufficient for synchronous control of several degrees of freedom (DoF) within modern multi-DoF prosthetics. In the FEM models activity across all fibre diameters is assumed, which provides a large signal, and is more representative of experimental conditions than neural prosthetics applications, where target activity may be limited to specific fibre diameter ranges. At the assumed signal, noise and error levels, SERs were sufficient for real-time imaging. For neural prosthetics, reconstruction of fascicle level activity with an estimated fraction change in impedance of -0.007 , representing activity in motor command fibres with a firing rate of 25 Hz, required a reduction in the noise and error values by a factor of 15 to 20 .

Implementation of EIT in nerve cuff has been successfully demonstrated by (Aristovich 2016, Aristovich 2017) in *in-vivo* bench-top experiments, using transverse current within a single electrode ring. A dual electrode ring requires stability in the alignment of the two electrode rings but otherwise may be implemented with much the same hardware. Chronic implantation of an EIT enabled nerve cuff would benefit from a stable impedance distribution of the passive tissues and any saline layer, provided by a stable nerve position within the nerve cuff, and from stability of the electrode tissue contact impedance.

A. Limitations of the modelling

The lumped-parameter and physiologically-detailed models of myelinated nerve fibre are approximations of a complex cytostructure, and may be improved using impedance measurements acquired directly from intra-fascicle tissue. The intra-fascicle tissue conductivity within the nerve FEM model may be improved by replacing the homogeneous fibre diameter distribution and significant fibre activity levels with, respectively, a heterogeneous fibre diameter distribution and variable levels of activity within fibre diameter groups. The assignment of the calculated intra-fascicle tissue conductivity as a bulk material property does not consider the true current paths through this tissue, which are affected, for example, by the relative locations of the nodes of Ranvier and the drive electrode pairs. Geometric considerations such as the electrode positions, which are assumed to be the same in two FEM models, would be subject to manufacturing tolerances during assembly of a real nerve cuff device. The models include noise, hardware errors, quantization, different mesh sizes and different conductivity distributions. However, while several measures have been taken to create synthesised data which is representative of real experimental data, the former is by no means a perfect substitute for the latter.

V. CONCLUSION

In this study we considered the application of EIT to a nerve cuff for recording neural activity by developing a model and then testing it using simulated data. The results in this study provide an estimate of the change in impedance of intra-fascicle tissue in mammalian nerve, and present a viable EIT drive and measurement electrode pattern, implemented on a dual-ring electrode array, to detect impedance changes in the anisotropic axis. These results are necessary steps towards implementing EIT in a nerve cuff and show extreme promise for developing advanced neural prosthetics interfaces.

REFERENCES

- Adler, A., R. Gaburro and W. Lionheart (2015). Electrical impedance tomography. *Handbook of Mathematical Methods in Imaging: Volume 1, Second Edition*: 701-762.
- Al-Shueli, A. I., C. T. Clarke, N. Donaldson and J. Taylor (2014). "Improved signal processing methods for velocity selective neural recording using multi-electrode cuffs." *IEEE Transactions on Biomedical Circuits and Systems* **8**(3): 401-410.

- Aristovich, K., Blochet, C., Avery, J., Donega, M., Holder, D. (2016). EIT of evoked and spontaneous activity in the peripheral nerve. 17th International Conference on BAEIT, Abstract Id: 235 www.eit2016.org.
- Aristovich, K., Donega, M., Perkins, J., Fjordbakk, C., Avery, J., Holder, D. (2017). In-vivo EIT imaging of spontaneous phasic activity in peripheral nerves. 18th International Conference on Biomedical Applications of Electrical Impedance Tomography. A. B. e. al. Thayer School of Engineering at Dartmouth, Hanover, New Hampshire, USA, <https://zenodo.org/record/557093#.WX5MkoSGM-U>.
- Aristovich, K. Y., G. S. Dos Santos and D. S. Holder (2015). "Investigation of potential artefactual changes in measurements of impedance changes during evoked activity: Implications to electrical impedance tomography of brain function." Physiological Measurement **36**(6): 1245-1259.
- Aristovich, K. Y., B. C. Packham, H. Koo, G. S. Santos, A. McEvoy and D. S. Holder (2016). "Imaging fast electrical activity in the brain with electrical impedance tomography." NeuroImage **124**: 204-213.
- Aristovich, K. Y., G. S. D. Santos, B. C. Packham and D. S. Holder (2014). "A method for reconstructing tomographic images of evoked neural activity with electrical impedance tomography using intracranial planar arrays." Physiological Measurement **35**(6): 1095-1109.
- Bayford, R., S. Ollmar, V. Mori, M. Oliveira, M. Vargas, A. da Cunha, R. de Souza, P. Pitrez and H. Moriya (2017). "16th International Conference on Electrical Bio-impedance and 17th International Conference on Biomedical Applications of Electrical Impedance Tomography (EIT)." Physiological Measurement **38**(6).
- Bayford, R. H. (2006). Bioimpedance tomography (electrical impedance tomography). Annual Review of Biomedical Engineering. **8**: 63-91.
- Biddiss, E., D. Beaton and T. Chau (2007). "Consumer design priorities for upper limb prosthetics." Disability and Rehabilitation: Assistive Technology **2**(6): 346-357.
- Boone, K. and D. Holder (1995). "Design considerations and performance of a prototype system for imaging neuronal depolarization in the brain using direct current electrical resistance tomography." Physiological measurement **16**(3A): A87.
- Boone, K. G. (1995). The possible use of applied potential tomography for imaging action potentials in the brain, University of London.
- Brazhe, A. R., G. V. Maksimov, E. Mosekilde and O. V. Sosnovtseva (2011). "Excitation block in a nerve fibre model owing to potassium-dependent changes in myelin resistance." Interface Focus **1**(1): 86-100.
- Chan, C. C., C. C. K. Lin and M. S. Ju (2012). "Estimation of ankle joint angle from peroneal and tibial electroneurograms a muscle spindle model approach." Journal of Mechanics in Medicine and Biology **12**(4).
- Choi, A. Q., J. K. Cavanaugh and D. M. Durand (2001). "Selectivity of multiple-contact nerve cuff electrodes: a simulation analysis." IEEE Transactions on Biomedical Engineering **48**(2): 165-172.
- Davidson, J., P. Wright, S. Ahsan, R. Robinson, C. Pomfrett and H. McCann (2010). fEITER—a new EIT instrument for functional brain imaging. Journal of Physics: Conference Series, IOP Publishing.
- del Valle, J. and X. Navarro (2013). Interfaces with the peripheral nerve for the control of neuroprostheses. International Review of Neurobiology. **109**: 63-83.
- Delgado-Martínez, I., J. Badia, A. Pascual-Font, A. Rodríguez-Baeza and X. Navarro (2016). "Fascicular topography of the human median nerve for neuroprosthetic surgery." Frontiers in Neuroscience **10**(JUL).
- Dowrick, T., C. Blochet and D. Holder (2015). "In vivo bioimpedance measurement of healthy and ischaemic rat brain: implications for stroke imaging using electrical impedance tomography." Physiological Measurement **36**(6): 1273.
- Dowrick, T., G. S. Dos Santos, A. Vongerichten and D. Holder (2015). "Parallel, multi frequency EIT measurement, suitable for recording impedance changes during epilepsy." Journal of Electrical Bioimpedance **6**(1): 37-43.
- Dumanian, G. A., M. A. McClinton and T. M. Brushart (1999). "The effects of free fat grafts on the stiffness of the rat sciatic nerve and perineural scar." The Journal of hand surgery **24**(1): 30-36.
- Engdahl, S. M., C. A. Chestek, B. Kelly, A. Davis and D. H. Gates (2017). "Factors associated with interest in novel interfaces for upper limb prosthesis control." PloS one **12**(8): e0182482.
- Fan, W., H. Wang and Z. Cui (2015). Damage detection of CFRP composites using open electrical impedance tomography. Conference Record - IEEE Instrumentation and Measurement Technology Conference.
- Farina, D., H. Rehbaum, A. Holobar, I. Vujaklija, N. Jiang, C. Hofer, S. Salminger, H.-W. van Vliet and O. C. Aszmann (2014). "Noninvasive, accurate assessment of the behavior of representative populations of motor units in targeted reinnervated muscles." IEEE Transactions on Neural Systems and Rehabilitation Engineering **22**(4): 810-819.
- Fouchard, A., V. Coizet, V. Sinniger, D. Clarençon, K. Pernet-Gallay, S. Bonnet and O. David (2017). "Functional monitoring of peripheral nerves from electrical impedance measurements." Journal of Physiology-Paris.
- Frerichs, I., M. B. P. Amato, A. H. Van Kaam, D. G. Tingay, Z. Zhao, B. Grychtol, M. Bodenstein, H. Gagnon, S. H. Böhm, E. Teschner, O. Stenqvist, T. Mauri, V. Torsani, L. Camporota, A. Schibler, G. K. Wolf, D. Gommers, S. Leonhardt, A. Adler, E. Fan, W. R. B. Lionheart, T. Riedel, P. C. Rimensberger, F. S. Sipmann, N. Weiler and H. Wrigge (2017). "Chest electrical impedance tomography examination, data analysis, terminology, clinical use and recommendations: Consensus statement of the TRanslational EIT developmeNt stuDY group." Thorax **72**(1): 83-93.
- Frijns, J. H. M. and J. H. ten Kate (1994). "A model of myelinated nerve fibres for electrical prosthesis design." Medical and Biological Engineering and Computing **32**(4): 391-398.
- Garai, P., R. G. L. Koh, M. Schuettler, T. Stieglitz and J. Zariffa (2017). "Influence of anatomical detail and tissue conductivity variations in simulations of multi-contact nerve cuff recordings." IEEE Transactions on Neural Systems and Rehabilitation Engineering **PP**(99): 1-1.
- Geada Trigo Calheiros De Figueiredo, J. (2014). The Role Of The Periaxonal Space In Sustained Impulse Conduction, UCL (University College London).
- Gielen, F. L. H., W. Wallinga-de Jonge and K. L. Boon (1984). "Electrical conductivity of skeletal muscle tissue: Experimental results from different muscles in vivo." Medical and Biological Engineering and Computing **22**(6): 569-577.
- Gilad, O., A. Ghosh, D. Oh and D. S. Holder (2009). "A method for recording resistance changes non-invasively during neuronal depolarization with a view to imaging brain activity with electrical impedance tomography." Journal of Neuroscience Methods **180**(1): 87-96.
- Graham, B. M. and A. Adler (2007). "Electrode placement configurations for 3D EIT." Physiological Measurement **28**(7): S29.
- Graimann, B. and H. Dietl (2013). Introduction to Upper Limb Prosthetics. Introduction to Neural Engineering for Motor Rehabilitation, John Wiley & Sons, Inc.: 267-290.
- Gun, L., D. Ning and Z. Liang (2017). "Effective Permittivity of Biological Tissue: Comparison of Theoretical Model and Experiment." Mathematical Problems in Engineering **2017**.
- Hamilton, S. J., M. Lassas and S. Siltanen (2014). "A direct reconstruction method for anisotropic electrical impedance tomography." Inverse Problems **30**(7): 075007.
- Haugland, M., A. Lickel, J. Haase and T. Sinkjaer (1999). "Control of FES thumb force using slip information obtained from the cutaneous electroneurogram in quadriplegic man." IEEE Transactions on Rehabilitation Engineering **7**(2): 215-227.
- Haugland, M. K. and J. A. Hoffer (1994). "Slip Information Provided by Nerve Cuff Signals: Application in Closed-Loop Control of Functional Electrical Stimulation." IEEE Transactions on Rehabilitation Engineering **2**(1): 29-36.

- Haugland, M. K., J. A. Hoffer and T. Sinkjær (1994). "Skin Contact Force Information in Sensory Nerve Signals Recorded by Implanted Cuff Electrodes." *IEEE Transactions on Rehabilitation Engineering* **2**(1): 18-28.
- Haugland, M. K. and T. Sinkjær (1995). "Cutaneous whole nerve recordings used for correction of footdrop in hemiplegic man." *IEEE Transactions on Rehabilitation Engineering* **3**(4): 307-317.
- Hodgkin, A. L. and A. F. Huxley (1952). "A quantitative description of membrane current and its application to conduction and excitation in nerve." *The Journal of Physiology* **117**(4): 500-544.
- Holder, D. S. (1992). "Impedance changes during the compound nerve action potential: Implications for impedance imaging of neuronal depolarisation in the brain." *Medical and Biological Engineering and Computing* **30**(2): 140-146.
- Holder, D. S. (2004). *Electrical impedance tomography: methods, history and applications*, CRC Press.
- Hope, J., Braeuer, B., Amirapu, S., McDaid, A., Vanholsbeeck, F. (2017). Extracting morphometric information from rat sciatic nerve using optical coherence tomography (OCT) – review and comparison of methods. *ANZCOP 2017*. Queenstown, NZ.
- Inmann, A. and M. Haugland (2004). "Implementation of natural sensory feedback in a portable control system for a hand grasp neuroprosthesis." *Medical Engineering and Physics* **26**(6): 449-458.
- Jabaley, M. E., W.H. Wallace, and F.R. Heckler (1980). "Internal topography of major nerves of the forearm and hand: A current view. ." *Journal of Hand Surgery* **5**(1): 1-18.
- Jabaley, M. E., W. H. Wallace and F. R. Heckler (1980). "Internal topography of major nerves of the forearm and hand: a current view." *The Journal of hand surgery* **5**(1): 1-18.
- Jehl, M., K. Aristovich, M. Faulkner and D. Holder (2016). "Are patient specific meshes required for EIT head imaging?" *Physiological Measurement* **37**(6): 879-892.
- Karimi, F. and S. R. Seydnejad (2015). "Velocity selective neural signal recording using a space-Time electrode array." *IEEE Transactions on Neural Systems and Rehabilitation Engineering* **23**(5): 837-848.
- Kuhn, A. (2008). *Modeling transcutaneous electrical stimulation*.
- Layton, B. and A. Sastry (2004). "A mechanical model for collagen fibril load sharing in peripheral nerve of diabetic and nondiabetic rats." *Journal of biomechanical engineering* **126**(6): 803-814.
- Liston, A., R. Bayford and D. Holder (2012). "A cable theory based biophysical model of resistance change in crab peripheral nerve and human cerebral cortex during neuronal depolarisation: Implications for electrical impedance tomography of fast neural activity in the brain." *Medical and Biological Engineering and Computing* **50**(5): 425-437.
- Liston, A. D. (2003). *Models and image: reconstruction in electrical impedance tomography of human brain function*, Middlesex University.
- McCann, H., S. T. Ahsan, J. L. Davidson, R. L. Robinson, P. Wright and C. J. Pomfrett (2011). "A portable instrument for high-speed brain function imaging: FEITER." *Conf Proc IEEE Eng Med Biol Soc* **2011**: 7029-7032.
- McIntyre, C. C., A. G. Richardson and W. M. Grill (2002). "Modeling the excitability of mammalian nerve fibers: influence of afterpotentials on the recovery cycle." *Journal of neurophysiology* **87**(2): 995-1006.
- McIntyre, C. C., A. G. Richardson and W. M. Grill (2002). "Modeling the excitability of mammalian nerve fibers: influence of afterpotentials on the recovery cycle." *J Neurophysiol* **87**.
- Morris, J. H., A. R. Hudson and G. Weddell (1972). "A study of degeneration and regeneration in the divided rat sciatic nerve based on electron microscopy." *Zeitschrift für Zellforschung und Mikroskopische Anatomie* **124**(2): 103-130.
- Nasehi Tehrani, J., A. McEwan, C. Jin and A. van Schaik (2012). "L1 regularization method in electrical impedance tomography by using the L1-curve (Pareto frontier curve)." *Applied Mathematical Modelling* **36**(3): 1095-1105.
- Neishabouri, A. and A. A. Faisal (2014). "Saltatory conduction in unmyelinated axons: clustering of Na⁺ channels on lipid rafts enables micro-saltatory conduction in C-fibers." *Frontiers in Neuroanatomy* **0**.
- Oh, T., O. Gilad, A. Ghosh, M. Schuettler and D. S. Holder (2011). "A novel method for recording neuronal depolarization with recording at 125-825 Hz: Implications for imaging fast neural activity in the brain with electrical impedance tomography." *Medical and Biological Engineering and Computing* **49**(5): 593-604.
- Ortiz-Catalan, M., R. Bråneemark, B. Häkansson and J. Delbeke (2012). "On the viability of implantable electrodes for the natural control of artificial limbs: Review and discussion." *BioMedical Engineering Online* **11**.
- Østlie, K., I. M. Lesjø, R. J. Franklin, B. Garfelt, O. H. Skjeldal and P. Magnus (2012). "Prosthesis rejection in acquired major upper-limb amputees: a population-based survey." *Disability and Rehabilitation: Assistive Technology* **7**(4): 294-303.
- Pannese, E. (2015). *Neurocytology: fine structure of neurons, nerve processes, and neuroglial cells*, Springer.
- Pollard, B. J., C. J. Pomfrett, A. Bryan, T. Quraishi, J. L. Davidson and H. McCann (2011). "Functional electrical impedance tomography by evoked response (fEITER): Sub-second changes in brain function during induction of anaesthesia with propofol: 7AP1-6." *European Journal of Anaesthesiology (EJA)* **28**: 97-98.
- Pomfrett, C., J. Davidson, R. Robinson, P. Wright, S. Ahsan, A. Bryan, B. Pollard and H. M. T. Quraishi (2010). "Functional Electrical Impedance Tomography by Evoked Response (fEITER): monitoring cerebral auto-regulation during the Valsalva manoeuvre."
- Prodanov, D. P. (2006). *Morphometric analysis of the rat lower limb nerves: anatomical data for neural prosthesis design*, University of Twente.
- Ranck Jr, J. B. and S. L. BeMent (1965). "The specific impedance of the dorsal columns of cat: An anisotropic medium." *Experimental Neurology* **11**(4): 451-463.
- Raspopovic, S., J. Carpaneto, E. Udina, X. Navarro and S. Micera (2010). "On the identification of sensory information from mixed nerves by using single-channel cuff electrodes." *Journal of NeuroEngineering and Rehabilitation* **7**: 17-17.
- Richardson, A. G., C. C. McIntyre and W. M. Grill (2000). "Modelling the effects of electric fields on nerve fibres: Influence of the myelin sheath." *Medical and Biological Engineering and Computing* **38**(4): 438-446.
- Rieger, R. and J. Taylor (2013). "A switched-capacitor front-end for velocity-selective ENG recording." *IEEE Transactions on Biomedical Circuits and Systems* **7**(4): 480-488.
- Scherer, S. S. and E. J. Arroyo (2002). "Recent progress on the molecular organization of myelinated axons." *Journal of the Peripheral Nervous System* **7**(1): 1-12.
- Silva, O. L., T. H. Sousa, I. O. Hoffman, E. D. de Camargo, F. S. de Moura, A. R. Martins, C. Biasi, D. T. Fantoni and R. G. Lima (2014). *A proposal to monitor muscle contraction through the change of electrical impedance inside a muscle*. Biomedical Robotics and Biomechanics (2014 5th IEEE RAS & EMBS International Conference on, IEEE.
- Spiers, A. J., L. Resnik and A. M. Dollar (2017). *Analyzing at-home prosthesis use in unilateral upper-limb amputees to inform treatment & device design*. 2017 International Conference on Rehabilitation Robotics (ICORR).
- Sunderland, S. (1945). "The intraneural topography of the radial, median and ulnar nerves." *Brain* **68**(4): 243-298.
- Taghipour-Farshi, H., J. Frounchi, N. Ahmadiasl, P. Shahabi and Y. Salekzamani (2015). "Effect of contacts configuration and location on selective stimulation of cuff electrode." *Bio-Medical Materials and Engineering* **25**(3): 237-248.
- Thompson, C. H., M. J. Zoratti, N. B. Langhals and E. K. Purcell (2016). "Regenerative Electrode Interfaces for Neural Prostheses." *Tissue Engineering - Part B: Reviews* **22**(2): 125-135.

1
2
3
4
5
6
7
8
9
10
11
12
13
14
15
16
17
18
19
20
21
22
23
24
25
26
27
28
29
30
31
32
33
34
35
36
37
38
39
40
41
42
43
44
45
46
47
48
49
50
51
52
53
54
55
56
57
58
59
60

Turovets, S., V. Volkov, A. Zherdetsky, A. Prakonina and A. D. Malony (2014). "A 3D finite-difference BiCG iterative solver with the fourier-jacobi preconditioner for the anisotropic EIT/EEG forward problem." Computational and Mathematical Methods in Medicine **2014**.

Tyler, D. J., K. H. Polasek and M. A. Schiefer (2015). Chapter 63 - Peripheral Nerve Interfaces A2 - Tubbs, R. Shane. Nerves and Nerve Injuries. E. Rizk, M. M. Shoja, M. Loukas, N. Barbaro and R. J. Spinner. San Diego, Academic Press: 1033-1054.

Vongerichten, A. (2015). Imaging Physiological and Pathological Activity in the Brain using Electric Impedance Tomography, UCL (University College London).

Vongerichten, A. N., G. S. dos Santos, K. Aristovich, J. Avery, A. McEvoy, M. Walker and D. S. Holder (2016). "Characterisation and imaging of cortical impedance changes during interictal and ictal activity in the anaesthetised rat." NeuroImage **124**: 813-823.

Wang, H., G. Xu, S. Zhang and W. Yan (2015). "An implementation of generalized back projection algorithm for the 2-D anisotropic EIT problem." IEEE Transactions on Magnetics **51**(3).

Weerasuriya, A., R. A. Spangler, S. I. Rapoport and R. E. Taylor (1984). "AC impedance of the perineurium of the frog sciatic nerve." Biophysical Journal **46**(2): 167-174.

Yoo, P. B. and D. M. Durand (2005). "Selective recording of the canine hypoglossal nerve using a multicontact flat interface nerve electrode." IEEE Transactions on Biomedical Engineering **52**(8): 1461-1469.

Yoshida, K., D. Farina, M. Akay and W. Jensen (2010). "Multichannel Intraneural and Intramuscular Techniques for Multiunit Recording and Use in Active Prostheses." Proceedings of the IEEE **98**(3): 432-449.

Zariffa, J. (2009). Bioelectric Source Localization in Peripheral Nerves, University of Toronto.

Zariffa, J. (2015). A review of source separation and source localization approaches in peripheral nerves. Conference Record - Asilomar Conference on Signals, Systems and Computers.

Ziegler-Graham, K., E. J. MacKenzie, P. L. Ephraim, T. G. Travison and R. Brookmeyer (2008). "Estimating the Prevalence of Limb Loss in the United States: 2005 to 2050." Archives of Physical Medicine and Rehabilitation **89**(3): 422-429.